Detecting tissue optical and mechanical properties with an ultrasound modulated optical imaging system in reflection detection geometry

Yi Cheng,[1] Sinan Li,[1] Robert J. Eckersley,[2] Daniel S. Elson,[3] and Meng-Xing Tang[1,*]

[1] Imperial College London, Department of Bioengineering, London, SW7 2AZ, UK
[2] King's College London, Department of Biomedical Engineering, London, SE1 7EH, UK
[3] Imperial College London, Hamlyn Centre for Robotic Surgery, Department of Surgery and Cancer, London, SW7 2AZ, UK
*mengxing.tang@imperial.ac.uk

Abstract: Tissue optical and mechanical properties are correlated to tissue pathologic changes. This manuscript describes a dual-mode ultrasound modulated optical imaging system capable of sensing local optical and mechanical properties in reflection geometry. The optical characterisation was achieved by the acoustic radiation force assisted ultrasound modulated optical tomography (ARF-UOT) with laser speckle contrast detection. Shear waves generated by the ARF were also tracked optically by the same system and the shear wave speed was used for the elasticity measurement. Tissue mimicking phantoms with multiple inclusions buried at 11 mm depth were experimentally scanned with the dual-mode system. The inclusions, with higher optical absorption and/or higher stiffness than background, were identified based on the dual results and their stiffnesses were quantified. The system characterises both optical and mechanical properties of the inclusions compared with the ARF-UOT or the elasticity measurement alone. Moreover, by detecting the backward scattered light in reflection detection geometry, the system is more suitable for clinical applications compared with transmission geometry.

©2014 Optical Society of America

OCIS codes: (170.1065) Acousto-optics; (110.0113) Imaging through turbid media.

References and Links

1. D. S. Elson, R. Li, C. Dunsby, R. Eckersley, and M.-X. Tang, "Ultrasound-mediated optical tomography: a review of current methods," Interface Focus **1**(4), 632–648 (2011).
2. X. Xu, H. Liu, and L. V. Wang, "Time-reversed ultrasonically encoded optical focusing into scattering media," Nat. Photonics **5**(3), 154–157 (2011).
3. M. X. Tang, D. S. Elson, R. Li, C. Dunsby, R. J. Eckersley, and P. N. T. Wells, "Photoacoustics, thermoacoustics, and acousto-optics for biomedical imaging," Proc. Inst. Mech. Eng. H **224**(2), 291–306 (2010).
4. L. V. Wang, "Mechanisms of Ultrasonic Modulation of Multiply Scattered Coherent Light: An Analytic Model," Phys. Rev. Lett. **87**(4), 043903 (2001).
5. E. Bossy, A. R. Funke, K. Daoudi, A.-C. Boccara, M. Tanter, and M. Fink, "Transient optoelastography in optically diffusive media," Appl. Phys. Lett. **90**(17), 174111 (2007).
6. C. Kim, R. J. Zemp, and L. V. Wang, "Intense acoustic bursts as a signal-enhancement mechanism in ultrasound-modulated optical tomography," Opt. Lett. **31**(16), 2423–2425 (2006).
7. Y. Li, H. Zhang, C. Kim, K. H. Wagner, P. Hemmer, and L. V. Wang, "Pulsed ultrasound-modulated optical tomography using spectral-hole burning as a narrowband spectral filter," Appl. Phys. Lett. **93**(1), 011111 (2008).
8. J. Li, G. Ku, and L. V. Wang, "Ultrasound-Modulated Optical Tomography of Biological Tissue by Use of Contrast of Laser Speckles," Appl. Opt. **41**(28), 6030–6035 (2002).
9. L. V. Wang, "Mechanisms of ultrasonic modulation of multiply scattered coherent light: a Monte Carlo model," Opt. Lett. **26**(15), 1191–1193 (2001).
10. A. P. Sarvazyan, O. V. Rudenko, and W. L. Nyborg, "Biomedical Applications of Radiation Force of Ultrasound: Historical Roots and Physical Basis," Ultrasound Med. Biol. **36**(9), 1379–1394 (2010).

11. R. Li, D. S. Elson, C. Dunsby, R. Eckersley, and M.-X. Tang, "Effects of acoustic radiation force and shear waves for absorption and stiffness sensing in ultrasound modulated optical tomography," Opt. Express **19**(8), 7299–7311 (2011).
12. M. L. Palmeri, A. C. Sharma, R. R. Bouchard, R. W. Nightingale, and K. R. Nightingale, "A finite-element method model of soft tissue response to impulsive acoustic radiation force," IEEE Trans. Ultrason. Ferroelectr. Freq. Control **52**(10), 1699–1712 (2005).
13. K. Nightingale, "Acoustic Radiation Force Impulse (ARFI) Imaging: a Review," Curr. Med. Imaging Rev. **7**(4), 328–339 (2011).
14. P. N. T. Wells and H.-D. Liang, "Medical ultrasound: imaging of soft tissue strain and elasticity," J. R. Soc. Interface **8**(64), 1521–1549 (2011).
15. J. K. Seo and E. J. Woo, "Magnetic Resonance Elastography," in *Nonlinear Inverse Problems in Imaging* (John Wiley & Sons, Ltd, 2013), pp. 335–353.
16. S. Song, Z. Huang, and R. K. Wang, "Tracking mechanical wave propagation within tissue using phase-sensitive optical coherence tomography: motion artifact and its compensation," J. Biomed. Opt. **18**(12), 121505 (2013).
17. Y. Cheng, R. Li, S. Li, C. Dunsby, R. J. Eckersley, D. S. Elson, and M.-X. Tang, "Shear Wave Elasticity Imaging Based on Acoustic Radiation Force and Optical Detection," Ultrasound Med. Biol. **38**(9), 1637–1645 (2012).
18. S. Li, Y. Cheng, L. Song, R. J. Eckersley, D. S. Elson, and M.-X. Tang, "Tracking shear waves in turbid medium by light: theory, simulation, and experiment," Opt. Lett. **39**(6), 1597–1600 (2014).
19. L. Wang, S. L. Jacques, and L. Zheng, "MCML--Monte Carlo modeling of light transport in multi-layered tissues," Comput. Methods Programs Biomed. **47**(2), 131–146 (1995).
20. H. J. van Staveren, C. J. M. Moes, J. van Marie, S. A. Prahl, and M. J. C. van Gemert, "Light scattering in Intralipid-10% in the wavelength range of 400-1100 nm," Appl. Opt. **30**(31), 4507–4514 (1991).

1. Introduction

Measuring optical and mechanical properties of biological tissue provides complementary information for clinical diagnosis. One challenge in medical optical imaging is the multiple scattering of light in tissue, which can severely degrade image resolution. To improve the image resolution at depth, several methods have been developed including ultrasound modulated optical tomography (UOT) [1], time-reversed ultrasonically encoded light focusing [2] and photo-acoustic tomography [3]. In UOT, part of the scattered light is modulated by focused ultrasound, e.g. the phase of the photons passing through the ultrasound focal region is modulated by the ultrasound as a result of refractive index change and displacement of optical scatterers [4], and the intensity of the ultrasound modulated light is selectively detected, either through the spectral features of modulated light [1] or based on the temporal features of speckles [5], to measure the optical properties within the ultrasound focal region [6–8]. Since ultrasound is much less scattered in tissue, the image resolution using the ultrasound modulated light may be improved to the size of ultrasound focus [9]. In addition to the ultrasound modulation, several studies have shown that the acoustic radiation force (ARF) - resulting from the momentum transfer from propagating ultrasound waves to the tissue - can increase the modulation by elevating the displacement of optical scatterers (in the order of µm) [10]. Using the laser speckle contrast detection method with properly adjusted exposure times of a charge-coupled device (CCD) camera, the ARF-assisted UOT is shown to increase the signal strength by 100% [11]. ARF itself has a well-defined focus which is comparable to the ultrasound focus [12]. However ARF-assisted UOT can have broadened lateral resolution if the optical measurement takes long and the measurement starts to contain shear wave effects.

Besides optical imaging, tissue elasticity imaging adds supplementary information for clinical diagnosis [13]. One way to quantitatively characterise tissue stiffness is to track shear wave propagation and the elasticity modulus can be calculated from the shear wave speed. Shear waves are usually detected by ultrasound and magnetic resonance imaging in tissue [14, 15]. Recently, it has been shown that shear waves can be tracked by light either using optical coherence tomography (OCT) for superficial tissue layers [16] or using laser speckle contrast analysis (SW-LASCA) of multiply scattered light at ~cm depths [17]. In [17], shear waves were generated a distance away from the laser axis. The propagation of shear waves to the optical detection volume increases the displacement of optical scatterers and thus the speckle

contrast difference (ΔC) recorded by a CCD camera [18]. The time-to-peak of the time-resolved CCD speckle contrast difference signal ΔC(t) indicates the time-of-flight of shear waves. With a transmission detection geometry, the shear wave speed was measured with 2 mm spatial resolution and the calculated phantom stiffness agreed well with an independent compression test (deviation less than 10%).

In this paper, it is the first study to show, as far as we are aware, that both optical information and quantitative elasticity information can be obtained using a single UOT system. It is also the first study to show that such dual information can be obtained in an optical reflection geometry. In the following sections, an experiment is described to produce one-dimensional (1D) UOT and elasticity measurements of tissue phantoms.
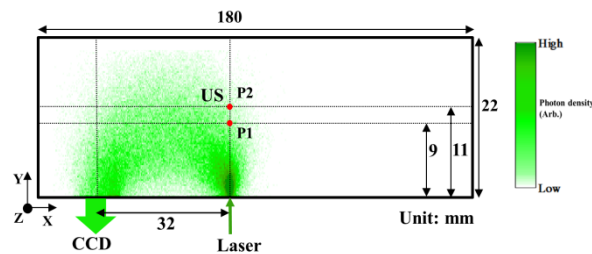
2. Experimental setup

Fig. 1. Top view of the experimental set-up. The rectangle depicts the cross-section of phantom which is 180 * 22 mm in size. The laser and the charge-coupled device (CCD) camera are positioned on the same side of the phantom and separated by 32 mm. The laser axis is in the y-direction, which is perpendicular to the CCD plane and the axis of the ultrasound (US) which lies along the z-axis. P1 and P2 are two US focal positions that lie on the laser axis and separated by 2 mm. The relative positions of P1 and P2 to the phantom surface were unchanged in the experiment. The green colouring represents the photon probability density found by Monte Carlo simulation [19], where darker colours indicate high photon density and thus high sensitivity of detection.

A 50 mW continuous wave 532 nm Nd:YAG laser (Excelsior 532, Newport Inc., Irvine, CA) and a CCD camera (QImaging Retiga EXi, Surrey, BC, Canada) were positioned 32 mm apart on the same side of tissue mimicking phantoms to collect the backward scattered photons (see Fig. 1). A 5 MHz focused ultrasound transducer (Parametric NDT Videoscan 307, Olympus, Essex, UK) was used to deliver 2 ms ultrasound bursts propagating perpendicular to the laser axis into the phantom. The ultrasound bursts not only modulated the photons passing through but also generated the ARF and the subsequent shear wave. Figure 1 shows the top view of the experimental system. The green area in the phantom is the simulated photon probability density of the scattered light (log-compressed) predicted by Monte Carlo simulation [19]. In the simulation, the optical absorption coefficient $\mu_a = 0.2\,cm^{-1}$, optical scattering coefficient $\mu_s = 30\,cm^{-1}$ and anisotropic coefficient g = 0.8, which were similar to the properties of the phantoms used in experiment [20]. As expected, a typical 'banana shape' light distribution is found where the highest photon probability density - indicating the most sensitive light detection area - is present near the laser source. P1 and P2 are two positions separating by 2 mm along the laser axis and also where the ultrasound bursts were focused. The ultrasound burst (and thus the ARF) was launched at separate times at P1 and P2, modulating the light passing through the ultrasound focal region and generating a shear wave propagating towards the light detection volume. The ultrasound and ARF modulated light and the shear wave modulated light were both detected with a time-resolved CCD speckle contrast difference signal ΔC(t) = C_{before}-C_{after} (t), where C_{before} is the background CCD speckle contrast acquired before the launch of the ultrasound burst, and C_{after} (t) is the CCD speckle contrast acquired with various time delays after the launch. The CCD speckle contrast C is defined as C = $\sigma/\langle I \rangle$,

where σ and ⟨I⟩ are the standard deviation and mean of the CCD pixel intensities respectively. At t = 0 ms, the signal (ΔC (0)) was acquired immediately after the ultrasound burst and before the spreading of the shear wave [12]. Therefore, it mainly resulted from the modulation of the ultrasound/ARF and was regarded as the UOT signal. The resolution of UOT was about 1 mm, that is, equal to the lateral width of the ultrasound focal region. As the propagation of the shear wave away from the ultrasound focal region, ΔC (t) was caused by the modulation of the shear wave and thus regarded as the signal of the SW-LASCA. Therefore, the separation of the ultrasound/ARF modulation and shear wave modulation was based on the CCD delay time. When the shear wave propagated to the most sensitive optical detection area (near the laser source), ΔC (t) peaked and the timing for the peak was related to the shear wave speed (explained in Section 4.1). In order to measure local shear wave speed, signals were acquired for both P1 and P2 and the difference of the timing of the peaks (Δt) in the two contrast difference signals indicated the time-of-flight of the shear wave between P1 and P2 (ΔS = 2 mm). The averaged shear wave speed between P1 and P2 was then simply calculated by $C_s = \Delta S/\Delta t$, and the shear modulus was calculated by $\mu = 3C_s^2\rho$, where $\rho = 1000$ kg/m3 was the density of the phantom.

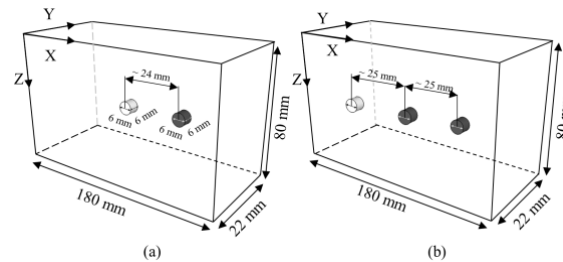## 3. Phantoms and data acquisition

Fig. 2. (a) Schematic of the two-inclusion heterogeneous phantom. The size of the phantom is 180 * 22 * 80 mm. The size of the inclusions is 6 mm in diameter and length. The distance between the inclusions is ~24 mm. The left inclusion is for mechanical contrast whereas the right is for optical (absorption) contrast. (b) Schematic of the three-inclusion heterogeneous phantom. The size of the phantom and the inclusions are the same as in (a). From left to right, the inclusions are for mechanical, optical and combined optical and mechanical contrast.

A 180*80*22 mm heterogeneous phantom was constructed with two cylindrical inclusions (6 mm diameter, 6 mm length, one mechanically stiff and one optically absorbing) separated by 24 mm and buried in the middle [Fig. 2(a)]. Figure 4(a) is a photo of the phantom cross section (X-Z plane). The surrounding medium was made of 0.8% agar powder and 4% intralipid solution. By adding extra 0.1% black ink the optical inclusion had a larger optical absorption coefficient, and the mechanical inclusion was made stiffer by increasing the agar powder concentration to 1.2%.

Another phantom was constructed with an additional third inclusion made of 1.2% agar powder, 4% intralipid solution and 0.1% black ink [Fig. 2(b) and Fig. 5(a)]. Thus, it had higher stiffness and optical absorption than the background. The size of the whole phantom and inclusions were the same as in the previous phantom while the distance between two adjacent inclusions was about 25 mm.

In a first experiment, the two-inclusion heterogeneous phantom was scanned twice with the ultrasound focused at P1 and P2, starting on the left side of the mechanical inclusion [Start point in Fig. 4(a)] and ending when the laser axis moved to the right side of the last inclusion [End point in Fig. 4(a)]. The 1D scans were recorded by stepping the phantoms with a 1 mm interval in the x direction for 60 mm while the ultrasound, the light and the CCD were stationary. At each position a contrast difference signal was acquired by delaying the 2 ms CCD exposure from 0 ms to 10 ms with a time step of 0.2 ms after the launch of the 2 ms

ultrasound burst. Due to the limitation of the CCD frame rate the data could not all be acquired for a single shear wave and instead multiple cycles were used with a delay between launching consecutive shear waves to allow for mechanical relaxation. The ultrasound peak-negative pressure at focus was 5.6 MPa and at each position the measurement was repeated three times. In a second experiment, the three-inclusion heterogeneous phantom was used and the same scanning scheme was adopted, but the phantom translation was 75 mm with 1 mm step size [Fig. 5(a)] and the ultrasound peak-negative pressure at focus was reduced to 4.4 MPa.

4. Results

4.1 UOT and SW-LASCA measurements

Figure 3 presents the time-resolved contrast difference signals detected when the ultrasound was focused at P1 (blue curve) and P2 (red curve) for a translation step without inclusion in the light volume. Both signals peaked when the shear wave reached the most sensitive optical detection volume. The signals at t = 0 ms [a1 and a2 in Fig. 3] were the UOT signals which resulted from the modulation of the ultrasound and ARF. The magnitude of a2 is smaller than that of a1 because P2 was further from the laser entry point than P1 and therefore fewer photons were modulated. The timing of the peaks of the two curves indicated by vertical dashed lines in Fig. 3 corresponds to the time at which the shear wave arrived the most sensitive detection volume. Therefore, the time difference (ΔT) was the time-of-flight of the shear wave between P1 and P2, which allows the shear wave speed to be calculated as the ratio of 2 mm and ΔT, and thus the distance between P1 and P2, which is 2 mm in the experiment, is the resolution of the SW-LASCA measurement.
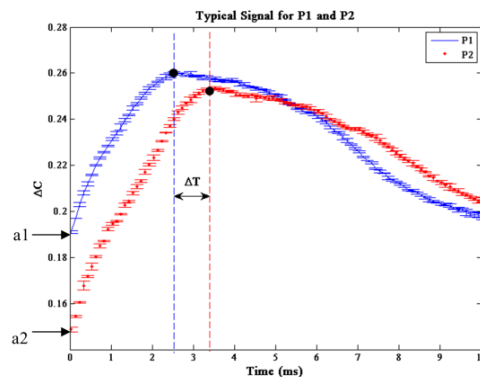

Fig. 3. Typical contrast difference signals for P1 and P2 at a certain position of the scan without any inclusion in the light volume. The blue curve is the time-resolved signal for P1 and the red curve is the signal for P2. The standard deviation was obtained by repeating measurement three times. a1 and a2 are the two values acquired at t = 0 ms and correspond to the modulation of ultrasound and ARF. ΔT is the time difference between the peaks of the two curves and indicates the time-of-flight of the shear wave between P1 and P2.

4.2 1D scan

The results of the 1D scan for the two-inclusion phantom are shown in Fig. 4(b) where the curve with dot markers is the UOT signal from P2 while the solid curve shows the stiffness of the phantom calculated using $\mu = 3C_s^2\rho$. The data when the ultrasound focus was at P2 was used as the UOT signal because it is 2 mm deeper than P1 in the phantom and better demonstrated the image depth of the UOT. The error bar at each scan position is the standard deviation from three repeated measurements at the same position. The positions of the

inclusions are indicated by the photo of the phantom cross section [Fig. 4(a)] and the shaded areas [Fig. 4(b)] in the figure.
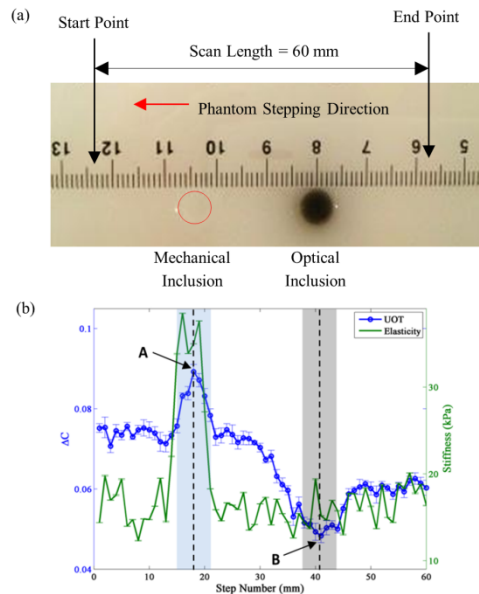

Fig. 4. (a) Photo of the cross section of the two-inclusion heterogeneous phantom. The red circle depicts the region of the mechanical inclusion and the black spot is the optical inclusion. The red arrow indicates the direction of the phantom stepping and the total stepping length is 60 mm with 1 mm step size. The start and end points for the scan are also shown in the figure. (b) 1D scan result for the two-inclusion heterogeneous phantom. The blue curve is the UOT signal when the ultrasound is focused at P2 and the green curve is the stiffness measurement. The standard deviation was from three repeated measurements at each step position. The positions of the inclusions are indicated by the shaded areas in the figure. A and B are the positions of the maximum and minimum contrast difference.

For the UOT measurement (blue curve), the signal alters within inclusions, increasing in the mechanical inclusion and decreasing in the optical inclusion. The two positions that bound the maximum range of contrast difference are marked as A and B respectively. The distance between A and B is 23 mm which is 1 mm different from the inclusion separation of 24 mm, but the resolution of the UOT measurement is about 1 mm, equal to the lateral width of the ultrasound focus region [6]. The full width at half maximum (FWHM) of the measurements for the two inclusions is 5.1 mm and 10.9 mm respectively. The FWHM is defined as the one-way distance between 50% of the maximum over the two baselines before and after the inclusion. The signal was firstly fitted by cubic interpolation and the FWHM was then calculated.

For the SW-LASCA measurement (green curve), the y-axis indicates the magnitude of the stiffness which increases within the mechanical inclusion but not in the optical inclusion, as expected. The FWHM of the mechanically affected region was found to be 4.9 mm which agrees well with 6 mm diameter of the mechanical inclusion considering the 2 mm resolution of the SW-LASCA measurement. Table 1 is a comparison between the stiffnesses measured in the experiment and in a previous study where the stiffnesses were obtained with an independent mechanical compression test [17]. As shown, the deviation between the optical (second column) and mechanical (third column) methods is no more than 10%.

Table 1. Stiffness of phantom measured with optical detection and an independent compression test

Phantom	Stiffness (optically)	Stiffness (mechanically)	Deviation
0.8% Agar	16.19 kPa	17.96 kPa	9.86%
1.2% Agar	34.12 kPa	35.47 kPa	3.55%

Figure 5 shows the dual results for the three-inclusion phantom where the blue curve shows the UOT signal and the green curve is the stiffness measurement. The error bars are the standard deviation of the three repeated measurements at each position. The UOT signal increased in the mechanical inclusion (FWHM 5.2 mm) and decreased in the optical inclusion (FWHM 10.1 mm) and combined mechanical and optical inclusion (FWHM 8.5 mm). The elasticity measurements showed the stiffness of the mechanical inclusion (FWHM 7.1 mm) and combined mechanical and optical inclusion (FWHM 4.6 mm) are higher than that of the optical inclusion and the background, as expected, again agreeing well with the 6 mm diameter of the inclusions considering the 2 mm resolution of the elasticity measurement. The three inclusions were easily identified and their qualitative optical absorption property and the quantitative mechanical property were obtained.
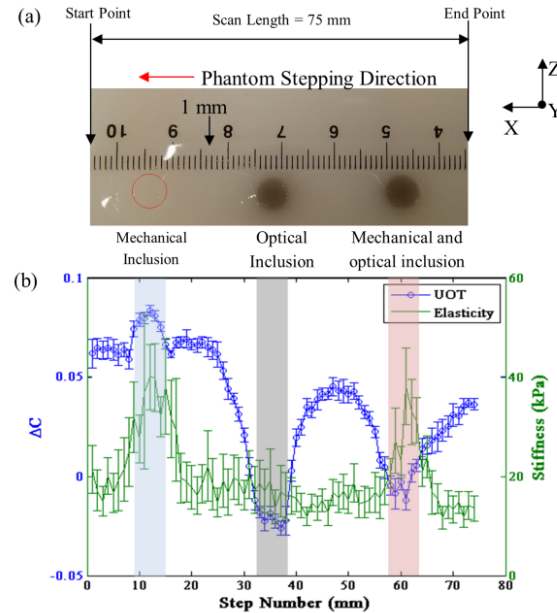

Fig. 5. (a) Photo of the phantom cross section where the three inclusions from the left to right are for mechanical (red circle), optical (dark spot) and combined mechanical and optical contrast (dark spot). They are separated by ~25 mm from each other. The red arrow indicates the phantom stepping direction and the total stepping length is 75 mm. (b) 1D scan results for the three-inclusion heterogeneous phantom. The blue solid curve with circular points is the UOT signal for P2 and the green solid line is the stiffness. The error bars are the standard deviations of three repeated measurements at each stepping position. The positions of the inclusions are indicated by the shaded areas in the figure.

5. Discussion and conclusion

By combining SW-LASCA with ARF-assisted ultrasound modulated optical tomography, we developed a dual-UOT system that quantitatively measures the elasticity and qualitatively provides optical absorption information at ~cm depth within tissue mimicking phantoms. The ability to measure both tissue elasticity and optical properties using the same hardware offers

a significant advantage over existing techniques in, e.g. imaging of cancer. The dual system was built in the reflection mode where laser and CCD camera were positioned on the same side of the samples. Due to the high degree of scattering of light in biological tissues, it may not be possible to take measurements in a transmission geometry and detection in reflection mode offers a more practical solution in such cases.

Only a simplified model of shear wave propagation is used in this study, while neglecting the reflection and possible interference of shear waves from multiple reflections on mechanical inclusion boundary, or the phantom boundary. This might add distortions to the $\Delta C(t)$ curve and needs to be further studied.

In Fig. 5, the ratio of the standard deviation and the UOT signal is larger than it in Fig. 4. The decreased signal-to-noise ratio is because of the reduced ultrasound pressure. The increased standard deviations of the stiffness measurement in Fig. 5 also result from the decreased ultrasound pressure. In Fig. 5, the UOT imaged optical absorber has a larger contrast with respect to the background and the mechanical inclusion than it in Fig. 4. This could be caused by the variation of the added black ink, which influences the absorption coefficient of inclusion and thus the signal amplitude.

In Figs. 4 and 5, within the mechanical inclusion, the UOT signal was expected to decline because the modulation from the ultrasound and ARF was expected to decrease in the mechanical inclusions where the displacement of the optical scatterers is smaller compared with the surrounding medium. Nevertheless it increases in both Fig. 4 and Fig. 5. Although there could be many factors affecting the result, one possible reason is that the photon modulation saturates in the softer background when the scatterer displacement induces phase change exceeds 2π. This needs to be further investigated

In Figs. 4 and 5, UOT signals neighbouring the optical inclusions do not stay on the baseline values. This is likely caused by the absorption of the scattered light by the optical inclusion, i.e. some photons were scattered into the optical inclusion and were absorbed even though the ultrasound focus was outside the inclusion (e.g. scan step 35 and 45 in Fig. 4). As a result, the UOT signal decreases due to the decrease of light intensity. This effect may be reduced by increasing the light intensity so that the decrease of detected photon has reduced influence on the UOT signal. In addition, the asymmetry in the UOT base line before and after the inclusions could be related with the uneven thickness of the phantom and the reflection detection of the CCD, which may change the light environment (e.g. the intensity and geometry) and thus the UOT baseline before and after the inclusion.

For future in vivo applications using this dual mode imaging system, a number of further improvements can be made. First of all, both of the system setup - including the separation and angle between the CCD and laser - and the measurement parameters - including the CCD exposure time and the length of the ultrasound burst - need to be optimised in order to obtain a good signal-to-noise ratio for clinic applications, e.g. in this study a measurement geometry of 180 degree back reflection was used. Considering future in vivo applications where the skin surface will be curved, a reflection geometry with an angle less than 180 degrees would be more appropriate, which could significantly reduce unmodulated optical background measurement and improve SNR. Secondly, the scan time can be significantly reduced by replacing the single element transducer used in this study with a phased array transducer with electronic focusing, and using a higher speed CCD camera for tracking the shear wave propagation. The use of an ultrasound system with a phased array transducer would also offer ultrasound B-mode images which can be naturally registered to the UOT and elasticity images. Thirdly, the green laser used in current study should be replaced by a near-infrared laser for a lower optical attenuation and thus a better penetration depth in biological tissues. Fourthly, speckle decorrelation needs to be investigated because it could lead to a noisy signal, e.g. it would be interesting to evaluate the influence of the speckle decorrelation on UOT and SW-LASCA measurements with a flow phantom. Fifthly, the resolution of the UOT measurement was estimated according to [6] which stated the resolution of an ARF-assisted

UOT is comparable with the ultrasound beam waist. With a hydrophone, we measured the ultrasound beam waist of our ultrasound transducer which is 1 mm. It would be useful to evaluate the resolution of our system by scanning a point scatter inclusion in phantoms in the future.

In summary, we have developed a dual-mode imaging system that is able to obtain both mechanical and optical information at ~cm depth on tissue-mimicking phantoms.

Acknowledgments